

# Ethanol-Based Solution Synthesis of a Functionalized Sulfide Solid Electrolyte: Investigation and Application

Yusuke Morino,<sup>\*[a]</sup> Kentaro Takase,<sup>[a]</sup> Kazuhiro Kamiguchi,<sup>[a]</sup> and Daisuke Ito<sup>[a]</sup>

A sulfide solid electrolyte was synthesized using a solution-phase approach via the dissolution of  $\text{Li}_3\text{PS}_4$  in ethanol followed by heat treatment (90–300 °C). This method yielded an electrolyte with a maximum lithium-ion conductivity of  $1.7 \times 10^{-5} \text{ Scm}^{-1}$  at 200 °C (down to 25 % of the pristine  $\text{Li}_3\text{PS}_4$ ); however, increasing the heating temperature resulted in a significant decrease in conductivity. Nuclear magnetic resonance spectroscopy revealed the decomposition of the  $\text{PS}_4^{3-}$  unit into  $\text{P}_2\text{S}_x$  dimers ( $\text{P}_2\text{S}_7^{4-}$  and  $\text{P}_2\text{S}_6^{4-}$ ) at high temperatures. X-ray absorption spectroscopy further confirmed a core-shell structure in the solution-phase-synthesized electrolyte, with an

enriched shell of oxygen-substituted  $\text{P}(\text{S}/\text{O})_x$  phases. Both the  $\text{P}_2\text{S}_x$  dimers in the core and the oxygen-rich shell may have contributed to the reduction in lithium-ion conductivity. Moreover, the oxygen-rich shell unexpectedly suppressed undesirable side reactions at the solid electrolyte/cathode interface. This study demonstrates the functionalization of solution-phase synthesis for sulfide solid electrolytes from ethanol, with a trade-off between conductivity and interface stability. Further optimizing the heat treatment process and shell engineering are promising avenues for enhancing the performance of all-solid-state batteries.

## Introduction

All-solid-state batteries (ASSBs) with inorganic solid electrolytes (SEs) are promising energy devices with excellent advantages, such as higher charge/discharge rates, longer lifetimes, and wider temperature ranges, compared to conventional liquid-electrolyte lithium-ion batteries.<sup>[1,2]</sup> Among the inorganic SEs, sulfide-based materials exhibit excellent formability at low temperatures and high lithium-ion conductivity. Sakuda et al.<sup>[3]</sup> reported that a dense body (relative density of > 90 %) could be formed via cold pressing in  $\text{Li}_2\text{S} - \text{P}_2\text{S}_5$  glass-ceramic SEs. Additionally, Kanno et al.<sup>[4]</sup> demonstrated that  $\text{Li}_{10}\text{GeP}_2\text{S}_{12}$  and its family exhibit conductivities exceeding  $10^{-2} \text{ Scm}^{-1}$ , comparable to those of traditional organic liquid electrolytes. These studies have accelerated the practical application of ASSBs with sulfide-based SEs.

One of the challenges in implementing ASSBs is the mass production of sulfide SEs. A general method for synthesizing SEs is solid-phase synthesis utilizing mechanical milling<sup>[5–7]</sup> and high-temperature heat treatment.<sup>[7–9]</sup> Particularly, several research groups have successfully synthesized high-performance sulfide SEs using mechanical milling.<sup>[10–12]</sup> Although these synthetic methods are highly suitable for fundamental studies and material development, they are impractical in mass production due to their reliance on batch processing. Hence, several liquid-phase synthetic methods that are more suitable for industrial applications have been proposed.<sup>[13–18]</sup>

Two types of liquid-phase synthetic approaches have been investigated including the use of a suspension system<sup>[13,14]</sup> or a complete solution.<sup>[14–18]</sup> An example of the suspension method is the “SEED method” proposed by Matsuda et al.,<sup>[13]</sup> which affords SEs by reacting a seed material ( $\text{Li}_2\text{S}$ ) with a solution containing other raw materials at the solid–liquid interface in the suspension. The complete solution method involves complete dissolution of the raw materials ( $\text{Li}_2\text{S}$  and metal sulfides) in a solvent, followed by drying with heating. Although the solution-phase synthetic method is simple and suitable for industrial purposes, several reports have indicated that the electrochemical properties, including lithium-ion conductivity, of synthesized SEs are highly dependent on the solvent used.<sup>[15–18]</sup> For example, Hayashi et al.<sup>[15,16]</sup> examined the lithium-ion conductivities of  $\text{Li}_3\text{PS}_4$  (LPS) glass-ceramics from ethylenediamine and N-methylformamide (NMF) solutions, which exhibited tenfold differences and conductivities of  $5.0 \times 10^{-5}$  and  $2.3 \times 10^{-6} \text{ Scm}^{-1}$ , respectively, at 25 °C. Additionally, Wissel et al.<sup>[17]</sup> investigated the dissolution and solution-phase synthesis of LPS in various solvents, such as alcohols, amides, nitriles, ethers, and aromatics, and determined that the NMF solution was promising. Both studies reported irreversibly mixed decomposed products, such as  $\text{Li}_3\text{PO}_4$ ,<sup>[15,17]</sup> in the SEs synthesized from alcohol solutions, which resulted in a lower lithium-ion conductivity compared to that of pristine LPS. Although both reports highlighted the low lithium-ion conductivity of SEs synthesized from alcohol solutions, they did not discuss the battery performance implications. The use of alcohol as a solvent in ASSB manufacturing offers several advantages, including easier controlled drying, reduced costs of material production, battery fabrication, and solvent recycling.

In this study, we synthesized LPS via dissolution in anhydrous ethanol (EtOH) followed by a heat treatment of 90–300 °C. The solution-phase-synthesized LPS samples were closely characterized using scanning electron microscopy (SEM),

[a] Y. Morino, K. Takase, K. Kamiguchi, D. Ito  
Murata Manufacturing Co., Ltd. 1-10-1 Higashikotari, Nagaokakyo-shi,  
Kyoto 617-8555, Japan  
E-mail: yusuke.morino@murata.com

 Supporting information for this article is available on the WWW under  
<https://doi.org/10.1002/batt.202400264>

electrochemical impedance spectroscopy (EIS), nuclear magnetic resonance (NMR) spectroscopy, and X-ray absorption spectroscopy (XAS). Furthermore, we demonstrated the use of an all-solid-state cathode half-cell that incorporated the solution-phase-synthesized LPS with EtOH and discussed the prospects of the solution-phase synthesis of sulfide SEs.

## Experimental Section

### Materials and Preparation

The test solutions were prepared using a sulfide SE in the form of an LPS powder and anhydrous EtOH as the solvent (purity > 99.5%), which were purchased from NEI (USA) and FUJIFILM Wako Chemicals (Japan), respectively. Material storage and all preparation procedures were conducted in an Ar-filled glove box (dew point of less than -80°C). The LPS/EtOH solution was prepared at 10 wt% and stirred at 25°C for 30 min (Figure 1). Subsequently, the yellow solution was dried for approximately 12 h at 90°C and heat-treated for 3 h at 150–300°C in the Ar-filled glove box. The heat-treatment temperatures were set at 90, 150, 200, 210, and 300°C. The samples were labeled pristine LPS and LPS@XXX °C (XXX=temperature of heat treatment). Every LPS sample for measuring the lithium-ion conductivity was weighed (80 mg) and pelletized in a 10-mmØ diameter zirconia cylinder via pressing at 300 MPa between SUS electrodes and restrained at 50 MPa in an airtight container.

### SEM

The particle size and morphology of the solution-phase-synthesized LPS were characterized via SEM observations. The SE particles were carefully dispersed and fixed onto a conductive carbon tape in an Ar-filled glove box. The samples were then transferred into a conventional SEM apparatus (S-4800, Hitachi Hi-Tech, Japan) without exposure to ambient air using an air-tight sample holder. The SEM images were obtained using an electron gun operated at an accelerating voltage of 5 keV in the secondary electron collecting mode.

### EIS

The lithium-ion conductivity of the samples was evaluated using EIS with a voltage amplitude of 30 mV in a frequency range of 10<sup>1</sup>–10<sup>5</sup> Hz at 22°C. The EIS plots were presented with normalized impedance considering the pellet thickness and electrode area (in Ω cm).

### NMR Spectroscopy

To evaluate the phosphorus-31 (<sup>31</sup>P) environment, the powdered samples that were prepared in the Ar-filled glove box were subjected to NMR spectroscopy. An AVANCEIII NEO spectrometer (Bruker, Germany) was employed using the single-pulse method at a Larmor frequency and magic angle spinning of 242.98 MHz and 12 kHz, respectively. The integration time was set with a repetition delay of 500 s, and sweeping was performed twice. Chemical shift referencing was conducted by fixing the peak position of the H<sub>3</sub>PO<sub>4</sub> solution at 0 ppm.

### XAS

To examine the P element state, P K-edge XAS spectra were obtained using the partial fluorescence yield (PFY) and total electron yield (TEY) methods in the beamline BL6 N1 at Aichi Synchrotron Radiation Center (Japan). The LPS powders were transferred to a vacuum analysis chamber in the absence of air. The PFY method offers an analysis depth of tens of micrometers, whereas the TEY method probes tens of nanometers. Therefore, it was possible to obtain non-destructive depth information on the chemical state of the samples. The PFY- and TEY-XAS spectra were processed using the ATHENA software package developed by Ravel et al.<sup>[19]</sup> The XAS spectra energy values were calibrated by aligning the white line peak position of Ca<sub>3</sub>(PO<sub>4</sub>)<sub>2</sub> at the P K-edge to 2152.2 eV to ensure an accurate interpretation of the XAS data.<sup>[20]</sup>

### Half-Cell Preparation

Half-cells of the In–Li | LiCoO<sub>2</sub> (LCO; Nippon Chemical Industrial Co., Ltd., Japan) system were prepared. In general, the cathode active material (CAM) is coated with LiNbO<sub>3</sub> or other oxides to ensure proper ASSB operation using a sulfide SE, similar to that reported by Ohta et al.<sup>[21]</sup> However, in this study, we deliberately prepared half-cells without coating to demonstrate the functionality of the above-mentioned solution-phase-synthesized LPS. The remaining cell fabrication process followed a standard procedure.<sup>[22–25]</sup> First, the cells were prepared by mixing SE/LCO at a volume ratio of 1:1 in a mortar with pristine LPS or solution-phase-synthesized LPS@200°C, following previous reports<sup>[22–25]</sup> confirming that this mixture ratio ensures sufficient cell operation. The half-cells comprised three layers: (i) a cathode mixture layer as the working electrode, which was designed to 2 mAh as calculated from the theoretical capacity. This included 13.3 mg of LCO (1 C-rate current defined to 2 mA); (ii) a Li<sub>6</sub>PS<sub>5</sub>Cl layer (NEI, USA) with 600 μm as the separator; and (iii) Li–In alloy as the counter electrode, which was designed to have a capacity approximately 30 times higher than that of the working electrode and maintained a constant potential of 0.62 V vs. Li<sup>+</sup>/Li throughout the experiment.<sup>[27]</sup> Because this potential is commonly used in studies that incorporate lithium electrodes, all potential values reported in this study were converted to "V vs. Li<sup>+</sup>/Li." The half-cells were fabricated by stacking the layers and pressing them together at 300 MPa, with further restraining at 50 MPa. The half-cell charging involved two steps: constant current (CC) charging at 4.25 V vs. Li<sup>+</sup>/Li at a 1/20 C-rate current, followed by constant voltage charging at 4.25 V vs. Li<sup>+</sup>/Li until the current attenuated to a 1/100 C-rate. Then, EIS measurements at the fully charged state were conducted. Subsequently, discharging was performed at CC (1/20 C-rate) until the voltage reached 3.0 V vs. Li<sup>+</sup>/Li. A 30-min rest period was included



Figure 1. Yellow solution of LPS/EtOH at 10 wt% following 30 min of stirring in an Ar-filled glove box.

between the charging and discharging cycles. This cell evaluation was performed in triplicate ( $n=3$ ), and the average value of the coulombic efficiency was calculated.

## Results and Discussion

The SEM images in Figure 2 indicate that the average particle size before (pristine) and after solution-phase synthesis remained nearly unchanged, ranging from 0.5 to 1  $\mu\text{m}$  in diameter. Therefore, further comparison of the electrochemical properties and chemical states of these SE samples followed.

Figure 3a shows the Nyquist and Bode plots at each heat-treatment temperature. The lithium-ion conductivity was calculated from the onset value of the EIS spectrum that corresponded to the capacitance component derived from the lithium-ion blocking electrodes. The lithium-ion conductivity of LPS@90°C (non-heat treated) could not be measured owing to its extremely high impedance. In the LPS@200°C sample, the conductivity attained a maximum value of  $1.7 \times 10^{-5} \text{ S cm}^{-1}$  followed by a decrease (Figure 3b). This maximum value was one-fourth that of pristine LPS, indicating that even at the peak conductivity produced by the solution-phase-synthesized LPS, the full reversibility of lithium-ion conduction may not be achievable. It is clearly observed in each EIS spectrum that at least one semicircular arc component exists in the high frequency region of  $10^4$ – $10^5$  Hz. It is well known that this collapsed semicircular arc component appears as the sum of the ionic conduction resistances of the bulk and SE/SE grain boundaries.<sup>[26]</sup> Therefore, several analytical techniques were employed to determine the heat-treatment temperature dependence and elucidate the spectral changes indicating the irreversibility of the lithium-ion conductivity.

Firstly, we investigated the NMR spectra of the pristine and solution-phase-synthesized LPS samples (Figure 4) and assigned peaks according to the systematic results of the NMR analysis obtained by Dietrich et al.<sup>[28,29]</sup> for Li<sub>2</sub>S–P<sub>2</sub>S<sub>5</sub> glass-ceramic SEs at various ratios. Jia et al.<sup>[30]</sup> also reported a similar NMR assignment for the Li<sub>2</sub>S–P<sub>2</sub>S<sub>5</sub> state change in response to pressure treatment. The P–S bond unit structures of PS<sub>3</sub><sup>-</sup>, P<sub>2</sub>S<sub>6</sub><sup>4-</sup>, P<sub>2</sub>S<sub>7</sub><sup>4-</sup>, PS<sub>4</sub><sup>3-</sup>, and P<sub>2</sub>S<sub>6</sub><sup>2-</sup> are observed in the NMR chemical shifts at 117, 104–107, 91, 87–89, and 55 ppm, respectively. Accordingly, the NMR spectra of the pristine LPS

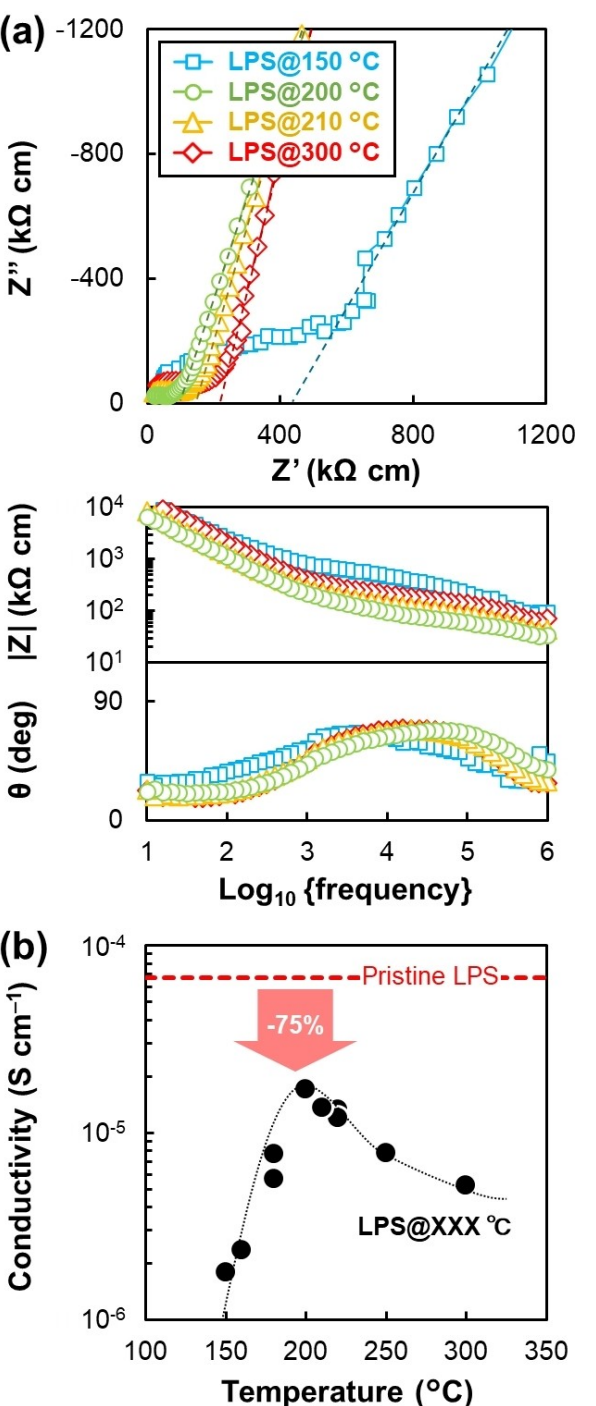


Figure 3. (a) Nyquist and Bode plots of LPS@150, 200, 210, and 300 °C. Each dotted line corresponds to fitting by capacitance component. (b) Change in lithium-ion conductivity with increasing temperature. The dashed line indicates the value for pristine LPS.

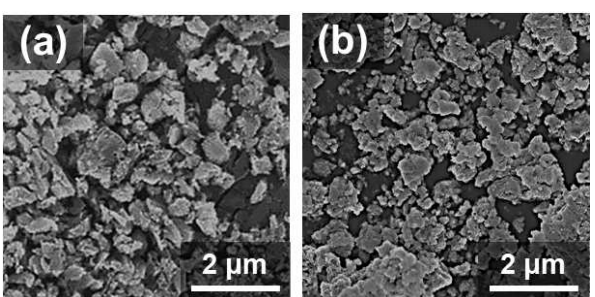


Figure 2. SEM observation with an electron gun at an accelerating voltage of 5 keV in secondary electron collecting mode. (a) Pristine LPS and (b) LPS@200 °C.

exhibited sharp peaks, indicative of a well-defined PS<sub>4</sub><sup>3-</sup> unit structure. The chemical states of the LPS@90°C samples predominantly showed a PS<sub>3</sub><sup>-</sup> chain structure, presumed to be the precursor structure in the EtOH solvent, with a minor presence of the PS<sub>4</sub><sup>3-</sup> tetrahedral unit (Figure 4b). After increasing the temperature to 150°C, PS<sub>3</sub><sup>-</sup> almost disappeared, and the major component gradually changed to PS<sub>4</sub><sup>3-</sup> and

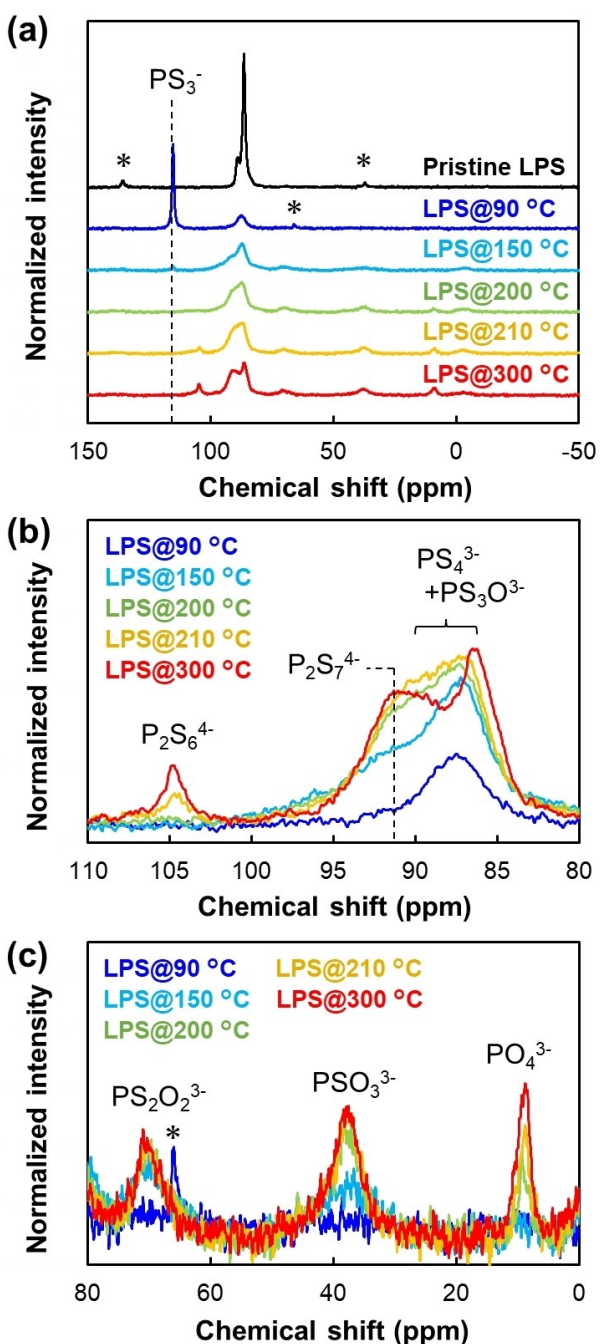


Figure 4. NMR spectra of the pristine and solution-phase-synthesized LPS samples of (a) the entire, (b) major component, and (c) minor component regions. The asterisks represent the spinning side bands of 12 kHz.

$\text{P}_2\text{S}_7^{4-}$ . In the LPS@200 °C samples,  $\text{PS}_3^-$  completely disappeared and the  $\text{PS}_4^{3-}$  and  $\text{P}_2\text{S}_7^{4-}$  peaks became more prominent. A significant improvement in the lithium-ion conductivity was observed in response to the change in the P–S bond unit structures, particularly after the disappearance of  $\text{PS}_3^-$ . This improvement was attributed to the  $\text{PS}_3^-$  skeleton,  $\text{Li}_2\text{P}_2\text{S}_6$ , with an extremely low lithium ionic conductivity (approximately  $10^{-11} \text{ S cm}^{-1}$  at 25 °C), as previously reported.<sup>[29]</sup> This was consistent with our experimental observation, being impossible to measure the lithium-ion conductivity of the LPS@90 °C

sample. Furthermore, the intensity of  $\text{P}_2\text{S}_6^{4-}$  increased, and a trace amount of  $\text{P}_2\text{S}_7^{4-}$  was detected in those heat-treated samples > 200 °C (Figure 4b). Moreover, the NMR peaks of the solution-phase synthesized LPS were broader than those of the pristine LPS, reflecting the low crystallinity of the former.

To assess the influence of the  $\text{P}_2\text{S}_x$  dimers on the lithium-ion conductivity, we compared our results with previously reported ones on  $\text{Li}_4\text{P}_2\text{S}_7$  and  $\text{Li}_4\text{P}_2\text{S}_6$ . The conductivities of  $\text{Li}_4\text{P}_2\text{S}_7$  and  $\text{Li}_4\text{P}_2\text{S}_6$  have been previously reported as  $10^{-5}\text{--}10^{-4} \text{ S cm}^{-1}$ <sup>[28,31-33]</sup> and  $10^{-10}\text{--}10^{-7} \text{ S cm}^{-1}$ <sup>[34,35]</sup>, respectively, indicating the low probability of  $\text{P}_2\text{S}_7^{4-}$  directly influencing and decreasing the lithium-ion conductivity in our experiments. The slight increase in  $\text{P}_2\text{S}_6^{4-}$  content was likely one of the factors increasing the lithium-ion conductivity at higher-temperatures. Additionally, the whole spectra of the solution-phase-synthesized LPS had broader peaks, thus implying that crystallinity was irreversible.

Three minor peaks at 71, 39, and 9 ppm, distinct from the major  $\text{P}_x\text{S}_y$  unit structures, were observed in the lower chemical shift region during high-temperature heat treatments (Figure 4c). In the LPS@150 °C samples, the peaks at 71 and 39 ppm were already present; however, the peak at 9 ppm was absent. In the LPS@300 °C samples, the peak at 71 ppm showed only a slight increase, whereas the peaks at 39 and 9 ppm were enhanced. In summary, the intensity of the lower chemical shift component was mostly positively correlated with the heat-treatment temperature. This trend could be explained by assigning these peaks (at 71, 39, and 9 ppm) to the oxygen-substituted units of  $\text{PS}_2\text{O}_2^{3-}$ ,  $\text{PSO}_3^{3-}$ , and  $\text{PO}_4^{3-}$ , respectively, which agreed with the results of Hayashi et al.<sup>[36]</sup>

Figure 5 shows the peak area ratio trends based on the NMR analysis, indicating the progression of the oxygen substitution of  $\text{PS}_4^{3-}$  into  $\text{P}(\text{S}/\text{O})_x$  as the temperature increased. This result was consistent with a previous study on solution-phase synthesis of LPS/alcohol systems reporting the production of phosphate upon heat treatment.<sup>[17]</sup> We therefore hypothesized that EtOH gas might be oxidizing the particle surface during desolvation.

Furthermore, the molecular dynamics simulation supported the assertion that the oxygen-substituted  $\text{P}(\text{S}/\text{O})_x$  species were more stable than  $\text{PS}_4^{3-}$  (Figure S1a in Supporting Information).

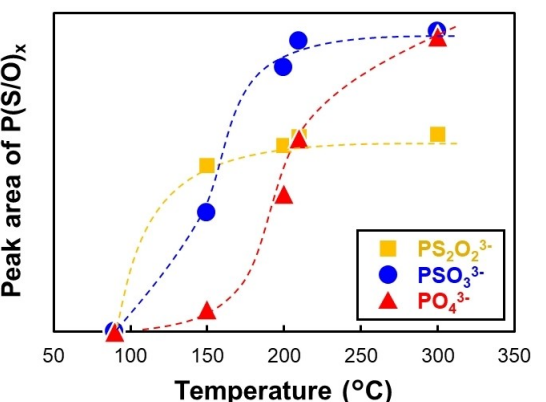
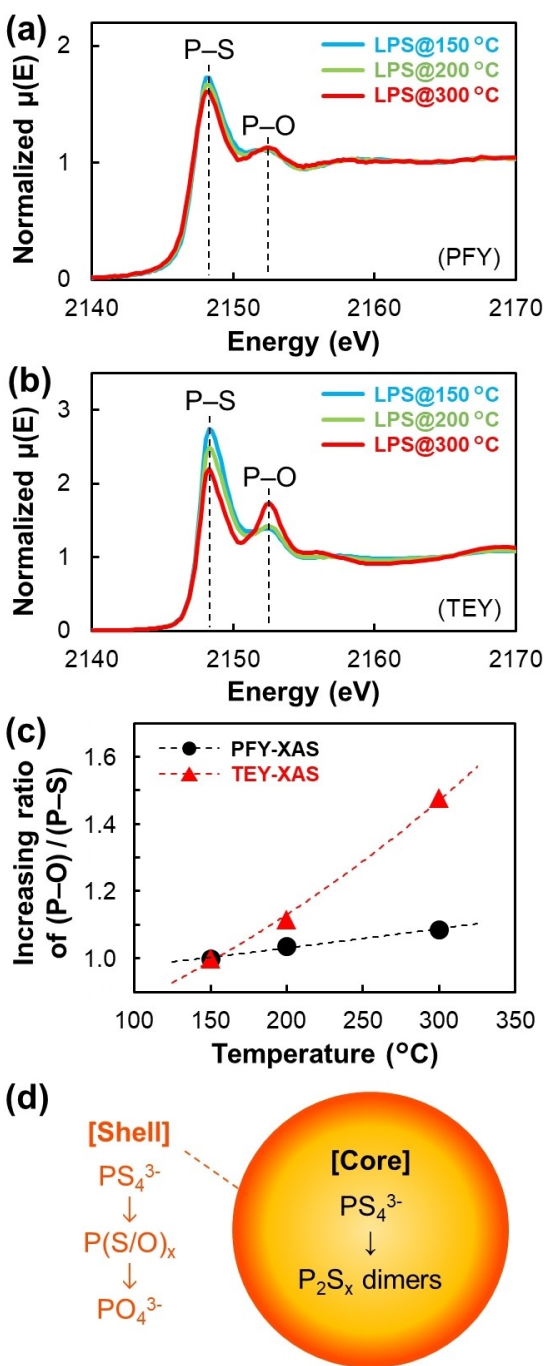


Figure 5. NMR peak area ratio of the minor components of  $\text{PS}_2\text{O}_2^{3-}$  (■),  $\text{PSO}_3^{3-}$  (●), and  $\text{PO}_4^{3-}$  (▲) shown in Figure 4c.

The oxygen-monosubstituted  $\text{PS}_3\text{O}^{3-}$  exhibited overlapping peaks with  $\text{PS}_4^{3-}$ <sup>[36]</sup> rendering the two species indistinguishable. The origin of the oxygen atom can be attributed to the hydroxyl group of EtOH, the trace amount of dissolved  $\text{H}_2\text{O}$  in EtOH, or the trace amount of residual gas in the Ar-filled glove box. However, its exact origin is difficult to be determined. Based on previous reports that have confirmed a dependence on solvent species, the hydroxyl group of EtOH is the most possible contributing factor.<sup>[29–31]</sup> Furthermore, Gamo et al.<sup>[14]</sup> suggested that the oxygen atom of the hydroxyl group in EtOH causes a substitution reaction with the sulfur in the raw  $\text{P}_2\text{S}_5$  material.

To evaluate the spatial distribution of the oxygen substitutes, XAS measurements were conducted on the LPS@150, 200, and 300 °C samples. Figures 6a and 5b show the XAS P K-edge spectra obtained via simultaneous measurements in the PFY and TEY modes. Depth information was captured on the PFY-XAS from a few to tens of micrometers, whereas TEY-XAS covered tens of nanometers. The simultaneous PFY- and TEY-XAS measurements enabled a non-destructive depth analysis. In both the PFY- and TEY-XAS spectra, two major peaks were observed at 2148 and 2152 eV (Figures 6a and b), which were assigned to P-S and P-O bonds, respectively.<sup>[20,25,37–40]</sup> Although the number of P-S bonds decreased and that of P-O increased as the heat-treatment temperature increased in both spectra, the increase in the P-O/P-S intensity ratio of the TEY-XAS spectra was more pronounced (Figure 6c). Combined with the NMR results, this phenomenon can be attributed to the oxygen-substituted components being locally generated in the region tens of nanometers away from the surface. The oxygen-substituted components reduced the lithium-ion conductivity,<sup>[36]</sup> finding that is confirmed by our computational simulation of lithium diffusivity for the  $\text{P}(\text{S}/\text{O})_x$  species (Figures S1b and S1c in Supplementary Information). Hence, in addition to the changes in the core  $\text{P}_x\text{S}_y$  structures, the localized oxygen substitution at the surface (like a shell structure) was a significant factor contributing to the decrease in lithium-ion conductivity with an increase in treatment temperature. The schematic shown in Figure 6d summarizes the findings from the NMR and XAS analyses and illustrates the core-shell structure of the solution-phase-synthesized LPS from EtOH.

Furthermore, the cathode half-cell performance was evaluated via the applications of the pristine and solution-phase-synthesized LPS samples (Figure 7). Numerous studies have revealed that the charge transfer barrier at the interface of uncoated cathode active material/sulfide SE significantly increases due to the formation of space-charge (depletion)<sup>[41–43]</sup> and elemental diffusion layers,<sup>[44,45]</sup> which results in charge-discharge performance deterioration with an increase in charge transfer resistance at the interface.<sup>[2,21–23,25,46]</sup> In accordance with previous studies, the capacity of the reference cell made from pristine LPS significantly deteriorated from the design capacity of 2 mAh. However, the cell constructed from the solution-phase-synthesized LPS@200 °C sample exhibited more pronounced charge/discharge curves despite the absence of a protective coating. This excellent electrochemical behavior could be attributed to the core-shell structure of the solution-phase-synthesized LPS, whose oxygen-substituted shell on the



**Figure 6.** XAS spectra in the (a) partial fluorescence yield (PFY) and (b) total electron yield (TEY) modes. The dashed lines correspond to P-S and P-O bonds, respectively.<sup>[20,25,37–40]</sup> (c) Increasing ratio of (P-O)/(P-S) in PFY (●) and TEY (▲) modes. (d) Schematic of the solution-phase-synthesized LPS at high-temperature treatments.

surface likely functioned as a buffering coating layer (Figure 8) when placed between LCO and the sulfide SE,<sup>[21–23]</sup> which was akin to  $\text{LiNbO}_3$ . Furthermore, the charge-discharge behavior can be explained by the charge transfer resistance value, which is approximately 10 times lower, as shown in Figure 7b.

The slope that was observed prior to a plateau at approximately 3.9 V vs.  $\text{Li}^+/\text{Li}$ , which corresponded to the redox potential of LCO, became shorter when the solution-phase-

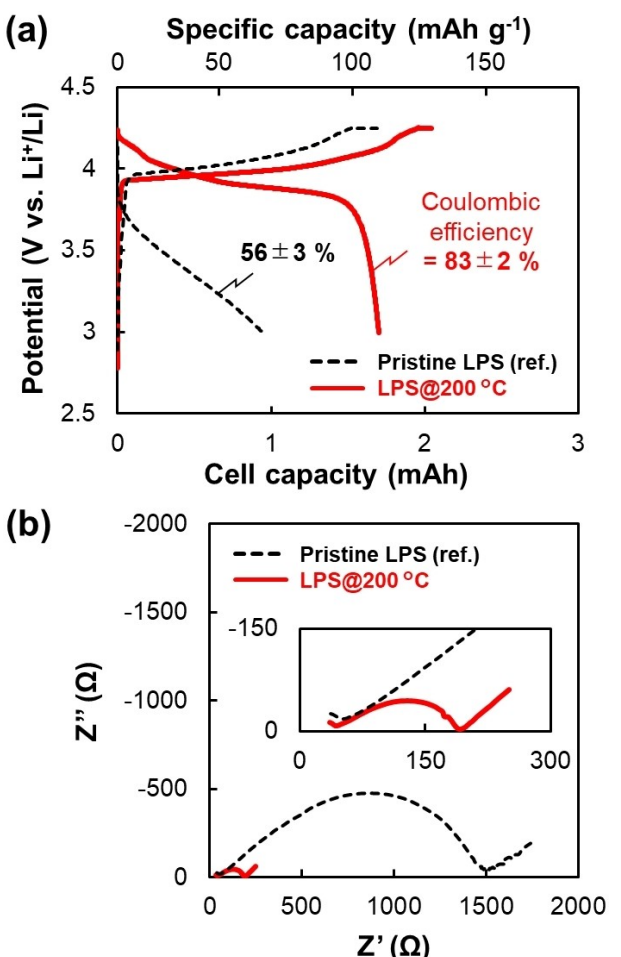


**Figure 7.** Cell performance of the cathode half-cell using LCO with pristine LPS (dashed black line) and solution-phase-synthesized LPS@200 °C (solid red line): (a) The first charge–discharge cycle and (b) EIS spectra at 4.25 V vs. Li<sup>+</sup>/Li in Nyquist plot form.

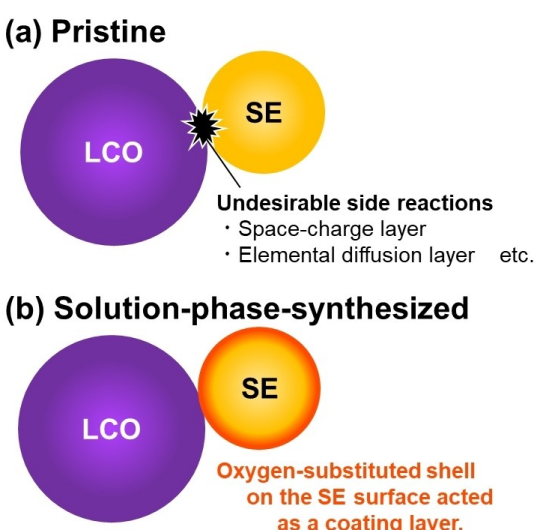


**Figure 8.** Differences in the charge/discharge curves in each case: (a) Pristine LPS and (b) solution-phase-synthesized LPS.

synthesized LPS was used at the beginning of the first charging cycle. Because the slope region was attributed to the side reactions between LCO and the sulfide SE,<sup>[21]</sup> a shorter slope region indicated the suppression of side reactions at the interface of LCO/SE, which was consistent with the above-mentioned observation. The effect of suppressing the interfacial side reaction of the elemental diffusion was also supported by our computational simulations, which suggested that the oxygen-substituted P(S/O)<sub>x</sub> unit was more thermodynamically stable at the LPS/LCO interface (Figure S2 of Supplementary Information). Accordingly, Banerjee et al.<sup>[47,48]</sup> experimentally revealed the thermodynamic stability of P(S/O)<sub>x</sub>. Thus, the performance of the cathode half-cell was improved in our experiment, despite the reduction of the lithium-ion conductivity of LPS to 25% via solution-phase synthesis from EtOH. Recent studies have reported the enhanced electrochemical stability of sulfide SEs via oxygen substitution.<sup>[49–52]</sup> Moreover, lithium-ion conductivity is an extremely important property for SE materials. Consequently, new and attractive liquid-phase synthetic methods have been recently proposed.<sup>[53–55]</sup> However, future studies should include a comprehensive approach to consider the additional functionalities of SE materials.

## Conclusions

In this study, we performed a solution-phase synthesis of the sulfide SE Li<sub>3</sub>PS<sub>4</sub> in EtOH, followed by heat treatment at various temperatures. The samples were characterized using EIS, NMR spectroscopy, and XAS. Although the maximum lithium-ion conductivity of 1.7×10<sup>-5</sup> Scm<sup>-1</sup> occurred at 200 °C, high temperatures resulted in a decreased conductivity due to the decomposition of the PS<sub>4</sub><sup>3-</sup> unit into P<sub>2</sub>S<sub>7</sub><sup>4-</sup> and P<sub>2</sub>S<sub>6</sub><sup>4-</sup> dimers and the formation of oxygen-substituted P(S/O)<sub>x</sub> phases. XAS results revealed that the solution-phase-synthesized SE exhibited a core-shell structure in the solution-phase synthesized material. Thus, we concluded that the P<sub>2</sub>S<sub>x</sub> dimers in the core and oxygen-rich shell reduced its lithium-ion conductivity. The lithium-ion conductivity of the heat-treated electrolyte was reduced to 25% compared to that of pristine LPS. Based on an evaluation of the cathode half-cell, the oxygen-rich shell suppressed undesirable side reactions by functioning as a coating layer at the interface of CAM and the sulfide SE. This functionalization highlights the potential of employing solution-phase synthesis for LPS from ethanol with a trade-off between conductivity and interface stability. Further optimization of heat treatments and shell engineering represent promising avenues for enhancing the performance of ASSBs.

## Conflict of Interests

The authors declare no conflict of interest.

## Data Availability Statement

The data that support the findings of this study are available from the corresponding author upon reasonable request.

**Keywords:** Sulfide solid electrolyte · Li<sub>3</sub>PS<sub>4</sub> · Solution-phase synthesis · NMR spectroscopy · X-ray absorption spectroscopy

- [1] P. Lu, Z. Zhou, Z. Xiao, J. Lu, J. Zhang, G. Hu, W. Yan, S. Xia, S. Zhang, Z. Wang, H. Li, C. Wang, F. Wu, X. Sun, *Joule* **2024**, *8*, 1–23.
- [2] P. Lu, Y. Wu, D. Wu, F. Song, T. Ma, W. Yan, X. Zhu, F. Guo, J. Lu, J. Peng, L. Chen, H. Li, F. Wu, *Energy Storage Mater.* **2024**, *67*, 103316.
- [3] A. Sakuda, A. Hayashi, M. Tatsumisago, *Sci. Rep.* **2013**, *3*, 2261.
- [4] Y. Sun, K. Suzuki, S. Hori, M. Hirayama, R. Kanno, *Chem. Mater.* **2017**, *29*, 5858–5864.
- [5] A. Hayashi, S. Hama, H. Morimoto, M. Tatsumisago, T. Minami, *J. Am. Ceram. Soc.* **2001**, *84*, 477–479.
- [6] K. Uchida, T. Ohkubo, F. Utsuno, K. Yazawa, *ACS Appl. Mater. Interfaces* **2021**, *13*, 37071–37081.
- [7] H. Kwak, K. H. Park, D. Han, K. Nam, H. Kim, Y. S. Jung, *J. Power Sources* **2020**, *446*, 227338.
- [8] S. Wang, Y. Zhang, X. Zhang, T. Liu, Y. H. Lin, Y. Shen, L. Li, C. W. Nan, *ACS Appl. Mater. Interfaces* **2018**, *10*, 42279–42285.
- [9] G. Sahu, Z. Lin, J. Li, Z. Liu, N. Dudney, C. Liang, *Energy Environ. Sci.* **2014**, *7*, 1053–1058.
- [10] K. Yamamoto, S. Yang, M. Takahashi, K. Ohara, T. Uchiyama, T. Watanabe, A. Sakuda, A. Hayashi, M. Tatsumisago, H. Muto, A. Matsuda, Y. Uchimoto, *ACS Appl. Energy Mater.* **2021**, *4*, 2275–2281.
- [11] L. Wu, Z. Zhang, G. Liu, W. Weng, Z. Zhang, X. Yao, *ACS Appl. Mater. Interfaces* **2021**, *13*, 46644–46649.
- [12] H. Chen, Y. Lu, H. Zhang, Y. Zhou, J. Chen, X. Huang, B. Tian, *Chem. Commun. (Camb.)* **2023**, *59*, 7220–7223.
- [13] R. Matsuda, E. Hirabara, N. H. H. Phuc, H. Muto, A. Matsuda, *IOP Conf. Ser. Mater. Sci. Eng.* **2018**, *429*, 012033.
- [14] H. Gamo, A. Nagai, A. Matsuda, *Batteries* **2023**, *9*, 355.
- [15] A. Ito, T. Kimura, A. Sakuda, M. Tatsumisago, A. Hayashi, *J. Sol Gel Sci. Technol.* **2022**, *101*, 2–7.
- [16] S. Teragawa, K. Aso, K. Tadanaga, A. Hayashi, M. Tatsumisago, *J. Mater. Chem. A* **2014**, *2*, 5095.
- [17] K. Wissel, L. M. Riegger, C. Schneider, A. I. Waidha, T. Famprakis, Y. Ikeda, B. Grabowski, R. E. Dinnebier, B. V. Lotsch, J. Janek, W. Ensinger, O. Clemens, *ACS Appl. Energy Mater.* **2023**, *6*, 7790–7802.
- [18] Y. Morino, M. Otoyama, T. Okumura, K. Kuratani, S. Takemoto, D. Ito, H. Sano, *ACS Appl. Mater. Interfaces* **2024**, *16*, 23169–23177.
- [19] B. Ravel, M. Newville, *J. Synchrotron Rad.* **2005**, *12*, 537–541.
- [20] L. C. C. Carlos, L. F. Francisco, W. O. Wedisson, L. Leonardus, J. Jörg, D. Dean, *Soil Syst.* **2019**, *3*, 61.
- [21] N. Ohta, K. Takada, L. Zhang, R. Ma, M. Osada, T. Sasaki, *Adv. Mater.* **2006**, *18*, 2226–2229.
- [22] Y. Morino, *Electrochemistry* **2022**, *90*, 27001.
- [23] Y. Morino, S. Kanada, *J. Power Sources* **2021**, *509*, 230376.
- [24] Y. Morino, *J. Power Sources* **2022**, *541*, 231672.
- [25] Y. Morino, A. Shiota, S. Kanada, W. S. K. Bong, K. Kawamoto, Y. Inda, H. Tsukasaki, S. Mori, Y. Iriyama, *ACS Appl. Mater. Interfaces* **2023**, *15*, 36086–36095.
- [26] Y. Morino, H. Sano, S. Kawaguchi, S. Hori, A. Sakuda, T. Takahashi, N. Miyashita, A. Hayashi, R. Kanno, *J. Phys. Chem. C* **2023**, *127*, 18678–18683.
- [27] A. L. Santhosha, L. Medenbach, J. R. Buchheim, P. Adelhelm, *Batteries & Supercaps* **2019**, *2*, 524–529.
- [28] C. Dietrich, D. A. Weber, S. J. Sedlmaier, S. Indris, S. P. Culver, D. Walter, J. Janek, W. G. Zeier, *J. Mater. Chem. A* **2017**, *5*, 18111–18119.
- [29] C. Dietrich, D. A. Weber, S. P. Culver, A. Senyshyn, S. J. Sedlmaier, S. Indris, J. Janek, W. G. Zeier, *Inorg. Chem.* **2017**, *56*, 6681–6687.
- [30] Z. Jia, X. Zhang, M. Qian, Y. Jin, Y. Xiong, *Chem. Eng. J.* **2022**, *435*, 134663.
- [31] M. Tachez, J.-P. Malugani, R. Mercier, G. Robert, *Solid State Ion.* **1984**, *14*, 181–185.
- [32] Z. Zhang, J. H. Kennedy, *Solid State Ion.* **1990**, *38*, 217–224.
- [33] M. Tatsumisago, F. Mizuno, A. Hayashi, *J. Power Sources* **2006**, *159*, 193–199.
- [34] C. Dietrich, M. Sadowski, S. Sicolo, D. A. Weber, S. J. Sedlmaier, K. S. Weldert, S. Indris, K. Albe, J. Janek, W. G. Zeier, *Chem. Mater.* **2016**, *28*, 8764–8773.
- [35] Z. D. Hood, C. Kates, M. Kirkham, S. Adhikari, C. Liang, N. A. W. Holzwarth, *Solid State Ion.* **2016**, *284*, 61–70.
- [36] A. Hayashi, H. Muramatsu, T. Ohtomo, S. Hama, M. Tatsumisago, *J. Alloys Compd.* **2014**, *591*, 247–250.
- [37] Y. Morino, H. Tsukasaki, S. Mori, *ACS Appl. Mater. Interfaces* **2023**, *15*, 23051–23057.
- [38] T. Hakari, M. Deguchi, K. Mitsuhashira, T. Ohta, K. Saito, Y. Orikasa, Y. Uchimoto, Y. Kowada, A. Hayashi, M. Tatsumisago, *Chem. Mater.* **2017**, *29*, 4768–4774.
- [39] X. Li, J. Liang, M. N. Banis, J. Luo, C. Wang, W. Li, X. Li, Q. Sun, Y. Hu, Q. Xiao, T.-K. Sham, L. Zhang, S. Zhao, S. Lu, H. Huang, R. Li, X. Sun, *Energy Storage Mater.* **2020**, *28*, 325–333.
- [40] I. Persson, W. Klysubun, D. A. Lundberg, *J. Mol. Struct.* **2019**, *1179*, 608–611.
- [41] J. Haruyama, K. Sodeyama, L. Han, K. Takada, Y. Tateyama, *Chem. Mater.* **2014**, *26*, 4248–4255.
- [42] B. Gao, R. Jalem, Y. Ma, Y. Tateyama, Y. Tateyama, *Chem. Mater.* **2020**, *32*, 85–96.
- [43] Y. Okuno, J. Haruyama, Y. Tateyama, *ACS Appl. Energy Mater.* **2020**, *3*, 11061–11072.
- [44] A. Sakuda, A. Hayashi, M. Tatsumisago, *Chem. Mater.* **2010**, *22*, 949–956.
- [45] J. Haruyama, K. Sodeyama, Y. Tateyama, *ACS Appl. Mater. Interfaces* **2017**, *9*, 286–292.
- [46] B. Gao, R. Jalem, Y. Tateyama, *ACS Appl. Mater. Interfaces* **2021**, *13*, 11765–11773.
- [47] A. Banerjee, H. Tang, X. Wang, J. H. Cheng, H. Nguyen, M. Zhang, D. H. S. Tan, T. A. Wynn, E. A. Wu, J. M. Doux, T. Wu, L. Ma, G. E. Sterbinsky, M. S. D'Souza, S. P. Ong, Y. S. Meng, *ACS Appl. Mater. Interfaces* **2019**, *11*, 43138–43145.
- [48] A. Banerjee, X. Wang, C. Fang, E. A. Wu, Y. S. Meng, *Chem. Rev.* **2020**, *120*, 6878–6933.
- [49] Z. Sun, Y. Lai, N. Lv, Y. Hu, B. Li, L. Jiang, J. Wang, S. Yin, K. Li, F. Liu, *ACS Appl. Mater. Interfaces* **2021**, *13*, 54924–54935.
- [50] L. Peng, S. Chen, C. Yu, C. Wei, C. Liao, Z. Wu, H. L. Wang, S. Cheng, J. Xie, *ACS Appl. Mater. Interfaces* **2022**, *14*, 4179–4185.
- [51] R. F. Indrawan, R. Matsuda, K. Hikima, A. Matsuda, *Solid State Ion.* **2023**, *401*, 116344.
- [52] R. Rajagopal, Y. Subramanian, Y. J. Jung, S. Kang, K. S. Ryu, *ACS Appl. Mater. Interfaces* **2023**, *15*, 21016–21026.
- [53] A. Han, R. Tian, L. Fang, F. Wan, X. Hu, Z. Zhao, F. Tu, D. Song, X. Zhang, Y. Yang, *ACS Appl. Mater. Interfaces* **2022**, *14*, 30824–30838.
- [54] R. Matsuda, H. Muto, A. Matsuda, *ACS Appl. Mater. Interfaces* **2022**, *14*, 52440–52447.
- [55] R. Rajagopal, Y. Subramanian, Y. J. Jung, S. Kang, K.-S. Ryu, *ACS Appl. Energy Mater.* **2022**, *5*, 9266–9272.

Manuscript received: April 17, 2024

Revised manuscript received: July 4, 2024

Accepted manuscript online: July 17, 2024

Version of record online: September 3, 2024